Computational and experimental study of intake ground vortices

S. Zantopp

D. MacManus
d.g.macmanus@cranfield.ac.uk

J. Murphy
Department of Aerospace Sciences,
School of Engineering, Cranfield University
Cranfield, UK

ABSTRACT

The ground vortices generated by an intake under both headwind and crosswind configurations have been investigated using computational and experimental approaches. The flow field of a scale-model intake was experimentally studied using stereoscopic particle image velocimetry to measure the ground vortex in conjunction with in-duct total pressure measurements for the internal flow. The computational predictions were performed using an unsteady Reynolds averaged Navier-Stokes approach. The experimental results show that under crosswind conditions a single ground vortex forms which becomes stronger as the crossflow velocity is increased. Under headwind conditions the measured ground vortex strength initially increases with freestream velocity before it reaches a local maximum and then reduces thereafter. The computations also exhibit the same characteristics and show good agreement with the measurements for some configurations. Based on the predictions, the complex flow field topology is investigated and a detailed flow model of the vortex flow field under crosswind conditions is proposed.

NOMENCLATURE

D	intake diameter [m]
D_l	intake highlight diameter [m]
DC_{60}	fan face total pressure distortion coefficient [-]
f	frequency [Hz]
h	height from ground plane [m]
H	intake centreline height [m]
M	Mach number [-]
n	Vatistas vortex model shape factor [-]

P	total pressure [Pa]
P_f	average fan face total pressure [Pa]
P_{60}	minimum average total pressure in a 60° sector [Pa]
q_f	average fan face dynamic pressure [Pa]
r	radial distance from centre of vortex [m]
r^*	non-dimensional radial distance, r/r_c [-]
r_c	vortex core size [m]
SC_{60}	fan face swirl distortion coefficient [-]
St	Strouhal number St $= (fD)/U_i$, [-]
t	time [s]
T_p	period of the fundamental oscillations [s]
U	velocity [ms^{-1}]
U_i	intake velocity [ms^{-1}]
U_θ	swirl velocity [ms^{-1}]
U^*	velocity ratio U_i/U_∞
y^+	non-dimensional wall distance [-]

Greek symbols

Γ	vortex circulation [m^{2}s^{-1}]
Γ^*	non-dimensional circulation $\Gamma/(D_1 U_i)$ [-]
δ^*	boundary layer displacement thickness [m]
ω	vorticity [s^{-1}]

Subscripts

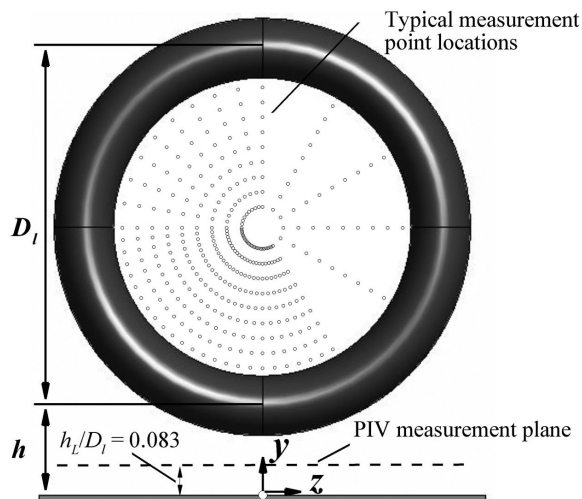|	
(x,y,z)	component aligned with (x,y,z) axis
∞	freestream conditions

Figure 1. Schematic of the SPIV and total pressure measurement arrangements for the crosswind configurations.

1.0 INTRODUCTION

When an aircraft engine operates in static or near-static conditions, a ground vortex can form between the surface and the engine intake. These vortices can be responsible for foreign object damage (FOD), compressor surge and total pressure distortion at the fan face which can lead to fan vibration. Although several research studies have been performed over the past 50 years, the detailed aerodynamics of the ground vortex, and its effect on the engine, are not fully understood. A number of control devices have been developed to reduce the potency of the ground vortex[1], but no such system is in current use. It is known that ground vortices can develop under most ambient wind conditions including headwind, crosswind and quiescent configurations. The design trend for turbofan configurations has been a steady increase in by-pass ratio and fan diameter. Consequently, for the conventional underwing architecture, the engines are placed non-dimensionally closer to the ground plane. Ground vortex formation and the vortex strength are known to depend on the ground clearance h/D and as this reduces, the vortex formation will occur over a much wider range of operating conditions. Hence, there is a need to understand the details of the aerodynamic mechanisms and the resulting vortex characteristics to reduce the possible risks associated with the vortex ingestion. It has been established previously that ground vortices can develop under a wide variety of ambient conditions and that the crosswind and tailwind conditions typically result in the most potent ground vortices[2]. Under crosswind conditions, a single strong vortex forms which is responsible for a notable total pressure distortion at the fan face. The effect of the ground vortex, can also be amplified by an induced intake lip separation if the crosswind velocity is sufficiently high[2]. Vortices under headwind and quiescent condition are generally less potent but still warrant careful consideration. Design rules with respect to ground vortex formation traditionally rely on the classic vortex criterion map[3], which is mostly based on flow visualisation and does not contain quantitative information about the vortex strength.

The formation mechanism under headwind and quiescent condition is reasonably well understood – although there is a lack of knowledge with regard to the quantification and the ensuing effect on the engine. Nevertheless, the formation mechanism is related to the concentration and amplification of ambient vorticity, which is mostly associated with the ground boundary layer of the approaching flow[4]. In the quiescent case, boundary layer development – and therefore vorticity production – is solely induced by the suction of the intake itself. The vortex system in this configuration is usually composed of two counter-rotating vortices, whose sense of rotation is determined by the dominant source of vorticity. However, even under headwind and quiescent conditions the quantitative aspect of the ground vortex is poorly understood. The crosswind mechanism is more complex and less well understood. The flow field consists of a strong ground vortex, which is accompanied by a trailing vortex system on the leeward side of the intake. In this configuration, the formation mechanism is different from that observed under quiescent and headwind conditions. The ground vortex develops even when the approaching crossflow is irrotational and therefore the main source of vorticity is not that associated with the approaching ground boundary layer.

The aim of this study is to use a combination of experimental and computational methods to understand the quantitative ground vortex characteristics and flow field as well as to assess the ability of the computational method to predict this complex flow. It investigates the main parameters which drive the vortex formation for both headwind and crosswind configurations and provides a broad set of validated quantitative data. Furthermore, it contributes to a deeper understanding of the formation mechanisms and the topology of the complex flow field associated with ground vortices.

2.0 EXPERIMENTAL FACILITIES, INSTRUMENTATION AND METHODS

Full details of the experiment apparatus, measurements and methodology are presented in Murphy[2]. The following sections provide a brief overview of some of the more pertinent aspects.

2.1 Wind tunnel and model

The experiments were conducted in the Cranfield University low-speed wind tunnel which has a 2·4 m × 1·8 m working section. The intake was an approximate 1/30th scale model of a modern high bypass engine with a circular, cylindrical geometry and a 0·1m inside diameter[2]. The outer diameter was 0·14m. The intake Reynolds number was fixed at $1·26 \times 10^6$ based on the inner diameter and the average intake velocity. Due to the low Reynolds number, transition strips were placed on both the inside and outside of the intake lip to promote transition and to avoid premature laminar separations. In addition, the lip geometry was modified relative to a large-scale intake and consisted of a 2:1 elliptical profile. A run time of approximately 20 seconds was achieved at a maximum mass flow of approximately 1·51kgs⁻¹ ($M_i = 0·58$) which had a typical variation of 0·1%. Total pressure measurements were taken at a location equivalent to a nominal aerodynamic interface plane (AIP) 0·7 D_i from the highlight plane. The pressure measurements were taken using a set of 40 Omega PX139-005D4V differential pressure transducers. Each pressure transducer has a range of ±5psi with typical repeatability of 0·1% full-scale and the measurements were acquired simultaneously. For each configuration, an acquisition time of five seconds was used with a sampling frequency of 600Hz. For each configuration, 432 total pressure measurements were obtained by rotating the model around its axis.

2.2 PIV system

A TSI stereoscopic PIV system was used to acquire the three velocity components on a plane. The PIV system consists of two four-mega pixel cameras used with 60mm focal length lens. The cameras were orientated at ±45° to the measurement plane with both operating in partial scatter with respect to the laser. A New Wave Solo 120XT Nd:Yag laser with a wave length of 532nm was used which provided a 1·5mm light sheet. The position of the light sheet relative to the intake is shown in Fig. 1. The resulting flow-field snapshots were acquired at a frame rate of 7·5Hz.

2.3 Experimental data processing

The PIV images were post-processed using TSI Insight3G software version 8.0.5. It was found that a deformation grid, along with the FFT algorithm was the best method to use for this flow-field. The method allows the procedure to be recursively implemented so that a multi-grid approach can be used to further increase the signal-to-noise ratio. A 64 × 64 interrogation spot was used initially with 50% overlap to maximise the correlation peak and ensure good sub-pixel accuracy in the displacement estimate for the window off-sets. A validation pass was also implemented which included a median filter to remove spurious vectors and 3 × 3 smoothing to remove any small scale noise present. The final iteration used a 32 × 32 (with 50% overlap) spot area to improve the resolution. This resulted in a measurement spatial resolution of 0·78mm.

For each configuration, 300 vortex snap-shots were obtained and for every snap-shot the vortex core was identified using the maximum vorticity magnitude. At the PIV plane, the vortex position, strength, Γ, and core size, r_c, was identified for each individual vortex snap-shot. The vortex strength of the primary ground vortex was determined by integrating all the vorticity of a particular sign over a circular domain with its centre being at the location of the vorticity peak. The positive and negative vortices were assessed separately. The vortex core size was identified using the vorticity disk method[5]. The output of this method is a circumferentially averaged swirl velocity distribution as a function of radial distance from the centre of the vortex:

$$U_\theta(r) = \frac{\Gamma(r)}{2\pi r} \qquad \qquad \dots (1)$$

The radial position of peak swirl velocity, $U_{\theta max}$, gives the vortex core size, r_c. Non-dimensionalising the swirl velocity distribution by the peak value, and the radial distance by the vortex core size, r_c, enables the Vatistas vortex shape factor, n, to be calculated using a least squares fit of the velocity distribution[6]. In the results presented below the average circulation has been obtained by averaging the values over all identified vortices over the 300 vortex snapshots. The time average flow field has been examined using the aligned vortex average technique (sometimes referred to as the conditional average[7]). This is where the vortex centre in each snapshot is spatially aligned and a temporal average of all the aligned vortex flow fields is then calculated. This technique removes the ambiguity associated with the conventional average technique (i.e. no vortex alignment) due to vortex wandering and unsteadiness. The same technique was used for both computational and experimental datasets.

The impact of total pressure distortion at the fan face was evaluated using the DC_{60} coefficient (Equation 2). It is defined as the difference between the average total pressure at the fan face and the minimum average total pressure in a 60° sector, non-dimensionalised by the average dynamic pressure.

$$DC_{60} = \frac{P_f - P_{60}}{q_f} \qquad \qquad \dots (2)$$

2.4 Measurement uncertainties

The measurement uncertainties comprise a combination of sources such as those due to the model location, transducers, random errors and the data acquisition system. Following the method of Taylor[8], these elements have been assessed to provide an estimate of the overall uncertainty for each measurement type.

The non-dimensional height was set with an uncertainty of $h/D_l = 0.25 \pm 3.6\%$. The free-stream velocity ranged from 10 to 50ms^{-1} with a typical overall uncertainty of ±1·1%. The intake velocity had an average value of 185ms^{-1} ±2·4%. The velocity ratio, U^*, ranged from ∞ to 4·6 and for a typical median velocity ratio of 6·1 the uncertainty

in U^* was ±2·64%. For the PIV velocity measurements an uncertainty band was estimated following the analysis presented by Raffel *et al*[9] which is based on synthetic PIV images. The correlation peak was estimated to be measured to within ±0·06 pixels for each camera. Misalignment of the light sheet with the calibration plate is expected to be the largest source of error, with the centre of the light sheet being, at worst ±0·25mm off centre. Using uncertainty estimates from Petracci *et al*[10] this is expected to result in a maximum error of 0·13 pixels. The total uncertainty is expected to be no worse than ±0·15 pixels. This equates to an in-plane velocity uncertainty of 1·61ms^{-1} or a typical error of ±3·2 %. Since the half-angle between the cameras was at 45°, the out of plane velocity error is equal to the in-plane error[11]. The vorticity uncertainty is estimated to be approximately ±1,875s^{-1} based on the maximum velocity error. This leads to a worst case uncertainty in the circulation of approximately ±0·3m^{2}s^{-1}. Further details on the uncertainty analysis and also the experiment apparatus and procedures are provided in Murphy[2].

3.0 THE COMPUTATIONAL METHOD
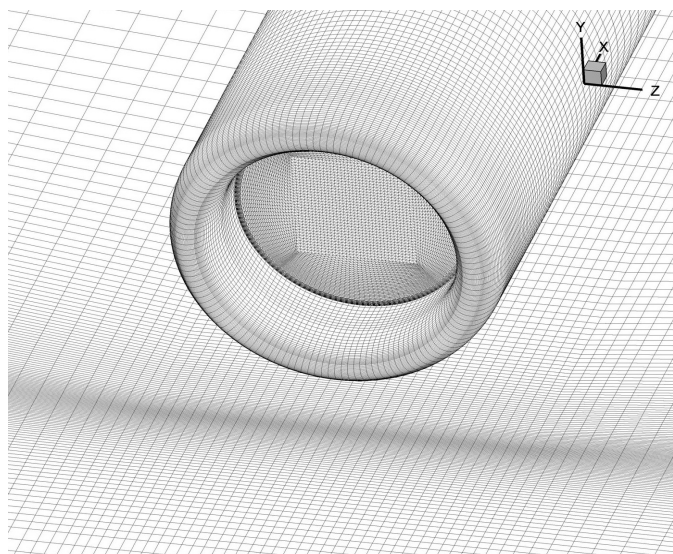
3.1 Computational grids

The geometry for the computational method corresponds to the intake model used in the experiment as described in the previous section. The non-uniform fully structured grid was generated using Pointwise Gridgen. It comprises 58 blocks and 2 million hexahedral cells. A wall function approach was adopted for the boundary layers and the appropriate $y+$ values were achieved by controlling the grid distributions normal to the no-slip walls. The overall computational domain is a rectangular prism with the dimensions $25D_l \times 25D_l \times 12\cdot5D_l$ in the streamwise, spanwise and ground normal directions (Fig. 2).

3.2 Solver

The three-dimensional flow field was predicted using Fluent Version 6.3 based on the solution of the Reynolds Averaged Navier Stokes (RANS) equations for a compressible, ideal gas. Spatial discretisation was performed using a third-order MUSCL scheme. The k-ω SST turbulence model was used in all cases. A fully implicit second order scheme was applied for temporal discretisation in unsteady calculations.

3.3 Boundary conditions

The domain size was chosen to be sufficiently large so that symmetry boundary conditions could be applied to the side faces of the domain without affecting the flow of interest (Fig. 2(b)). For the headwind configurations, the upstream boundary was specified as a pressure inlet where the total pressure profile and total temperature were specified. Furthermore, during the experiment, the approaching boundary-layer velocity profile was measured in the wind tunnel. This profile was applied at the inlet face to ensure that the CFD predictions were performed using the same boundary layer characteristic as in the experiments. The domain exit was a pressure outlet boundary condition where the static pressure was specified to deliver the required freestream velocity. The intake suction flow was generated by also using a pressure outlet boundary condition at the exit of the duct. The required static pressure was determined iteratively to match the massflow condition from the experiment and thereby deliver the specified velocity ratio. The calculations were performed in parallel with the experimental investigations and consequently there are small differences between the final experimental and computational velocity ratios. This is because subsequent to the wind tunnel tests, small corrections were applied to both the
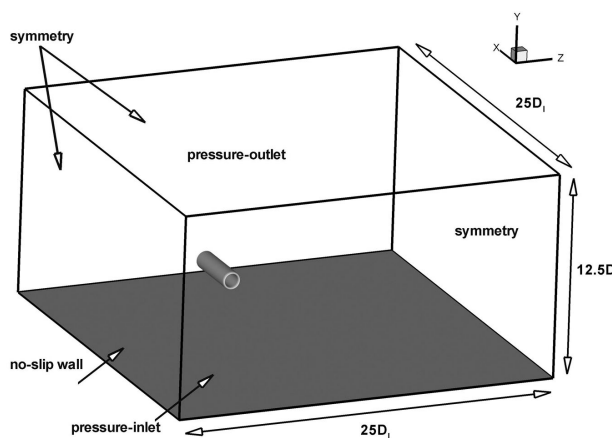
(a)

Figure 2. (a) Structured grid topology around the intake, (b) computational domain and boundary conditions for the headwind calculations.

freestream velocity as well as the suction massflow measurement. The differences are small and do not hamper the comparisons between the predictions and the measurements.

3.4 Convergence studies

Grid convergence studies have been performed following the method of Roache[12] which is based on a theory of general Richardson extrapolation. Solutions were obtained with three different levels of grid spacing using a constant grid refinement ratio. As the flow physics is different for headwind and crossflow configurations, the grid convergence studies were performed for both types of flow modes. The grids comprised approximately 0·90, 1·39 and 2·14m cells each. The y^+ targets were maintained for each configuration and the grids were not uniformly refined between each level. Overall the grid sensitivity studies showed that the main metric of interest – i.e. the vortex strength – is only slightly affected by grid refinement with a maximum change of 4·7% in the vortex total circulation between the coarse and fine grids. Furthermore, the predicted vortex core radius in the PIV plane decreases as the spatial

resolution is refined. Further investigations of the actual order of accuracy and grid convergence indices (GCI) based on the vortex characteristics presented implausible results. The reason for this could not be fully evinced, but two main issues have been identified. Richardson extrapolation is based on the assumption of uniform grid refinement, which is difficult to realise when dealing with non-uniform grids where it is particularly clustered in a specific region and with additional requirements in terms of non-dimensional wall-distance. Complexity of the flow field associated with the ground vortices may be another issue. For example, Karlsson & Fuchs[13] showed, that the flow field of headwind ground vortices has several transient modes. Green observed 'indications of hysteresis and multiple solutions to the same boundary conditions'[14] in his CFD study. These two aspects are not believed to affect the obtained solutions significantly, but as grid convergence studies are sensitive to small changes, these issues may result in a breakdown of the theoretical model. All of the presented computational results were obtained with the fine grid in order to reduce discretisation errors as far as possible.

3.5 Error statement

Iterative convergence was satisfactory in most of the investigated configurations as indicated by residuals in the order of 10^{-5}. However, in crosswind cases with a high freestream velocity, it was not always possible to achieve residual levels below 10^{-3}, due to significant flow separation at the inlet lip. However, even in these cases the vortex characteristics of size, position, and strength iteratively converged to a steady value.

3.6 Computational data processing

To ensure comparability between the experimental and computational data, both data sets have been processed in the exact same way. According to the method described in Section 2.3, the computational dataset is used to derive the fundamental vortex characteristics in the PIV plane. The vortex position is identified using the location of maximum vorticity magnitude. Vortex strength is obtained by integrating positive (or negative) vorticity over a circular domain with its centre in the vortex core. The experimental PIV data was acquired on a grid with a spatial resolution of 0·78mm. The CFD grid was different and non-uniform. To enable a fair comparison for validation purposes with the CFD data, the computational results are interpolated onto the same circular grid used for the second-stage of PIV processing. Although this inherently reduces the resolution of the CFD data it enables the integral vortex circulation to be directly compared.

In the general case, the DC_{60} coefficient as described in Section 2.3 (Equation (2)) will be dominated by the total pressure loss which arises from the vortex ingestion. Although there are limitations associated with DC_{60} there are no established alternative parameters and it is therefore used as a metric of flow distortion in this work. As vortex ingestion also affects the velocity distribution in terms of swirl, the computational data have also been used to derive a further distortion coefficient based on swirl velocity (Equation (3)).

$$SC_{60} = \frac{\left|U_{\theta,60}\right| - \left|U_{\theta,f}\right|}{U_x} \qquad \qquad \ldots (3)$$

It is defined as the difference between the maximum average absolute swirl velocity in a 60° sector and the average absolute swirl velocity at the fan face, non-dimensionalised by the average axial velocity in the duct. This definition is slightly different from what proposed by Green[15], where the sign of the swirl velocity was taken into account rather than using the absolute value. For the application to flow fields containing vortical structures the definition shown in Equation (3) appears to be more useful as vortex ingestion always arises with both negative and positive swirl components.
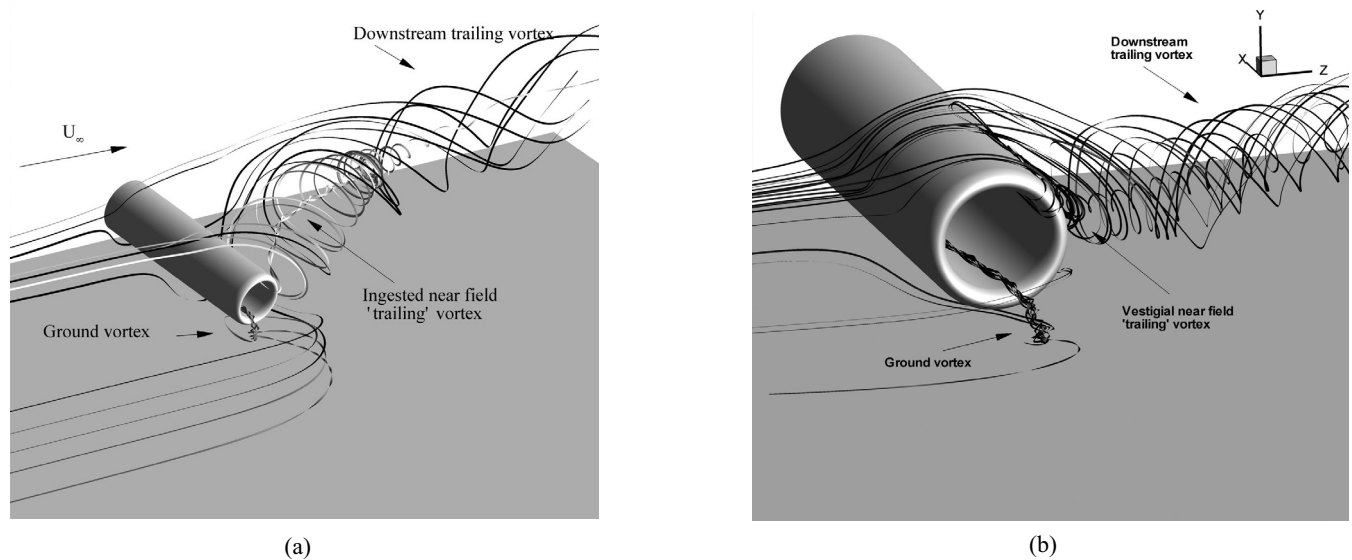
(a)   (b)

Figure 3. Predicted streamlines for crosswind configurations with $h/D_l = 0.25$ (a) $U^* = 19.8$ (b) $U^* = 5.7$.
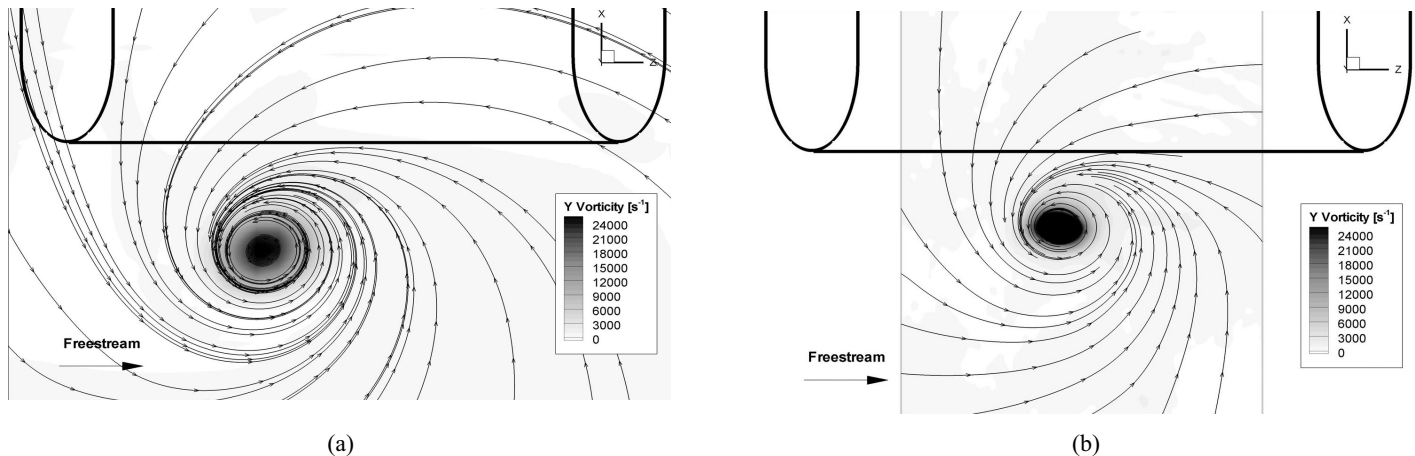

(a)   (b)

Figure 4. Flowfield in the PIV Plane (top view) showing a comparison between the CFD predictions
(a) and PIV measurements (b) for a crosswind configuration ($U^* \approx 19.8$, $h/D_l = 0.25$).

4.0 CROSSWIND RESULTS AND DISCUSSION

4.1 Basic flow features and topology

For a ground vortex to arise, the sucked streamtube must be large enough so that it interacts with the ground. Under typical crosswind conditions, a strong ground vortex is ingested into the intake at the point closest to the ground i.e. at around the 6 o'clock position. Once ingested, its trajectory within the intake rolls slightly in a circumferential direction towards the windward side as a result of the interaction of the vortex and the wall of the inlet duct. The ground vortex is accompanied by a trailing vortex which is observed on the leeward of the intake (Fig. 3(a)). The trailing vortex is also ingested into the intake and has a much larger diameter in the leeward region. The experimental results showed that this strong crosswind ground vortex is relatively steady in both magnitude and position. Similarly the CFD predictions showed no significant unsteadiness for these

configurations. A comparison between the CFD and quantitative experimental measurements shows that there is reasonably good agreement in the magnitude, position and size of the ground vortex as illustrated in the example shown in Fig. 4. The predicted vortex is larger than the measured one and the peak vorticity is slightly lower. The lateral position agrees well although there is small difference in the distance from the highlight. The CFD predictions also show that the ground vortex vorticity originates around the intake surface as well as partially from the ground plane. A prediction using a slip wall on the ground surface showed that the ground vortex strength (circulation) increased by about 8% but that the vortex location was unaffected. This supports the previously reported observations[4] that the crosswind ground vortex characteristics are primarily unaffected by the approaching or suction induced ground vorticity.

The near ground flow topology is also investigated by visualising the surface streaklines based on the predicted surface skin friction vectors. As expected, this shows a system of separation and reattachment lines, saddle points, nodes and focal points (Fig. 5). It clearly identifies the ground vortex focal point (F1) as well as the
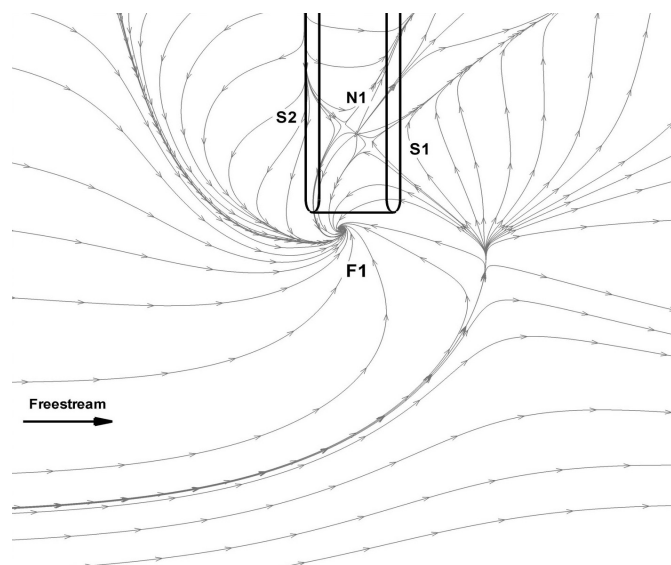
Figure 5. Plan view of the predicted ground plane surface streaklines for a crosswind configuration ($U^* = 19\cdot8$, $h/D_l = 0\cdot25$).

Figure 6. Predicted streamlines for a crosswind configuration showing two near-field trailing vortices ($U^* = 5\cdot0$, $h/D_l = 0\cdot25$).

bounding streakline and attachment point associated with the edge of the sucked streamtube. The flow structure in the near field and between the intake and the ground is more complex. Upstream of the intake is a separation line which terminates at the ground vortex focal point (F1). Directly underneath the intake is a nodal point (N1) as well as a pair of saddle points (S1, S2). On the leeward side there are two separation lines which are associated with the trailing vortex. This system is a result of complex interactions due to the sucked streamtube as well as the effects of the approaching ground boundary layer, the suction induced ground flow and the flow around the cylinder[2].

The term 'trailing vortex' is commonly used in the literature to describe the downstream leg of the intake vortex system. There are no quantitative measurements of this trailing vortex and all of the studies to date have used relatively simple flow visualisation methods. Detailed investigation of the predicted structure of the vortex shows that it is not a classical trailing vortex such as that generated by a finite lifting wing. In this case, the vortex is ultimately ingested by the intake and previous studies have failed to clearly identify the vorticity source associated with this feature. In terms of the trailing vortex topology, the postulated flow models presented in de Siervi et al[4] depict the vortex emanating on the leeward edge of the intake and travelling downstream through the sucked streamtube. However a flow topology such as this seems unlikely since this would require the continuous trailing vortex to pass through the sucked streamtube boundary. The current CFD predictions reveal a more complex – but more credible – flowfield topology. For a non-dimensional height (h/D_l) of 0·25 and a velocity ratio (U^*) of 19·8, a single ground vortex forms between the intake and the ground plane (Fig. 3(a)). However, at this velocity ratio there are two trailing vortices; one inside (denoted by near field) and one outside the sucked streamtube (Fig. 3(a)). The nearfield trailing vortex is associated with the vorticity on the intake outer surface. This vorticity initially travels downstream and once the edge of the capture streamtube is reached, it is convected back towards the intake. This reverse flow forms the core flow of the trailing vortex. This can be seen from the near field ribbon streamline patterns in Fig. 3(a). The far field downstream trailing vortex is associated with the flow that travels over the outside of the captured streamtube. This trailing vortex also includes vorticity which originates from the outer intake surface as well as from the ground plane on the leeward side of the intake (Fig. 3(a)) and is weaker than the 'ingested'
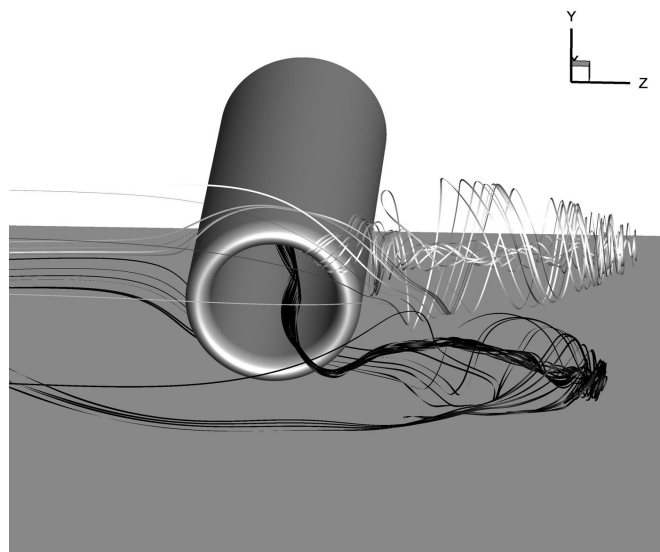
trailing vortex. Computations at a lower velocity ratio (U^*) of 5·7 also show a complex arrangement of three vortices – two of which are ingested into the intake (Fig. 3(b)). A close inspection of the flow reveals that there is a vestigial near-field 'trailing' vortex but that it is very small and does not extend significantly downstream (Fig. 3(b)). This vortex is also ingested into the intake. As the velocity ratio is reduced to a critical value ($U^* = 5\cdot0$), the sucked streamtube is no longer large enough to interact with the ground plane and the ground vortex switches to having a second trailing vortex on the leeward side of the intake (Fig. 6). The uppermost trailing vortex moves slightly towards the top position of the intake, so that the pair of vortices is roughly located at 1 and 5 o'clock position at the intake.

4.2 Crosswind vortex circulation and in-duct distortion

Quantitative comparisons with the experimental data focus on two main aspects. Firstly, the total vortex circulation in the PIV measurement plane and secondly, the DC_{60} coefficient based on total pressure distortion at the fan face. A range of CFD predictions were performed for the crosswind configurations and the ground vortex was observed for velocity ratios (U^*) of 19·8, 9·9 and 5·7. Predictions for U^* of 5·0 and 4·0 showed that the sucked streamtube does not intersect the ground and consequently the ground vortex was not predicted to occur. In these cases, two ingested 'trailing' vortices are predicted as previously illustrated in Fig. 6. Within the intake, the flow distortion is affected by both the ingested vortices as well as the possible crosswind separation on the windward lip. The CFD predictions capture both of these aspects and there is reasonable topological agreement with the experimental measurements (e.g. Fig. 7). The predicted ingestion location agrees well with the measurements although the CFD typically underpredicts the level of total pressure loss at the vortex core. It also shows the size and strength of the crosswind lip separation which occurs under these conditions. This large windward side lip separation region is predicted to reduce and eventually disappear as the velocity ratio increases which is in agreement with the measurements[2]. As the lip separation reduces with an increasing velocity ratio (U^*), the ingested ground vortex reduces in strength and the loss core position moves towards the crosswind side in a clockwise direction.

$U_i/U_\infty = 6.1$

$U_i/U_\infty = 5.7$

$U_i/U_\infty = 9.1$

$U_i/U_\infty = 9.9$

$U_i/U_\infty = 18.3$ $\psi = 90°$
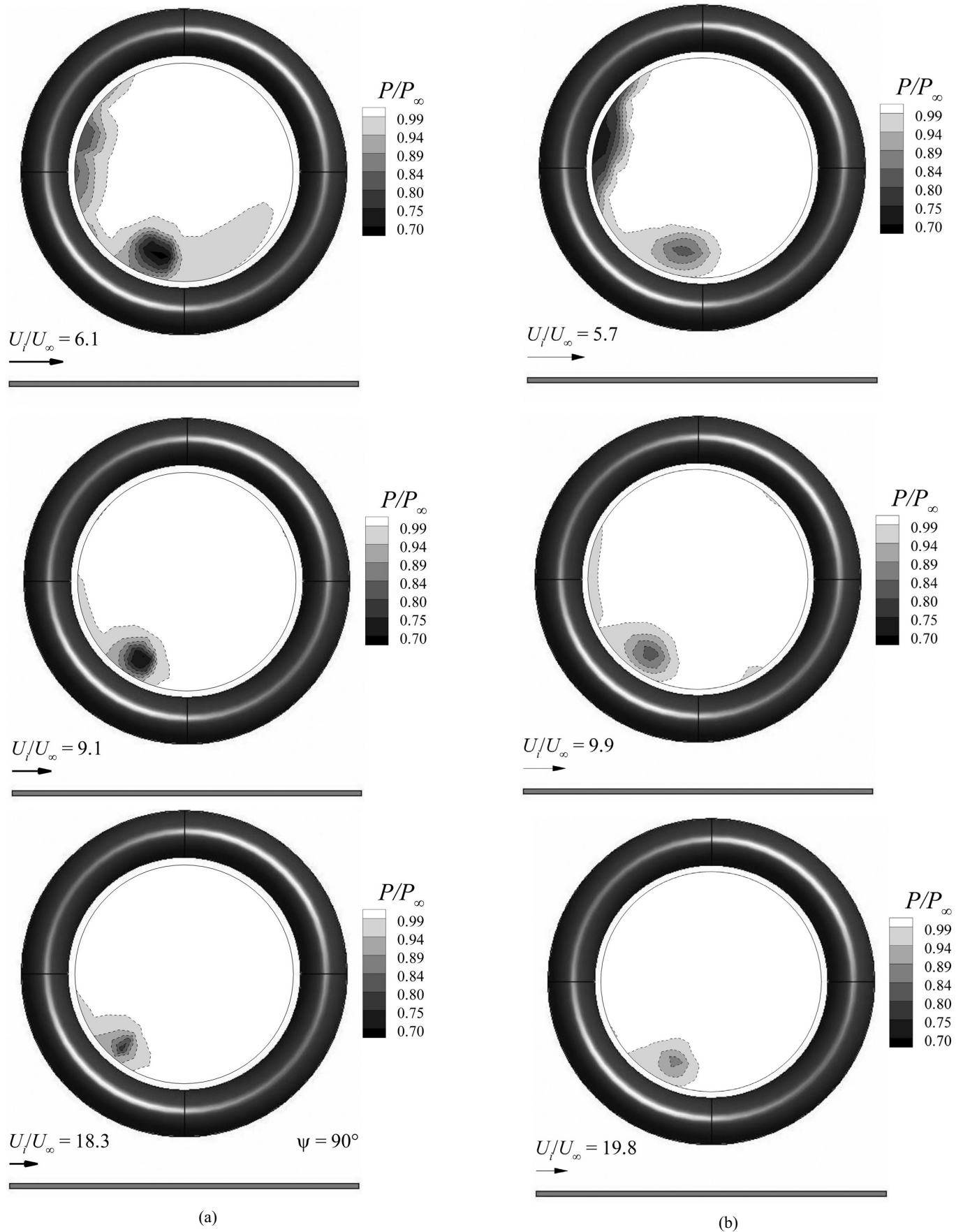
$U_i/U_\infty = 19.8$

(a)

(b)

Figure 7. Total pressure distribution in the AIP under crosswind conditions comparing
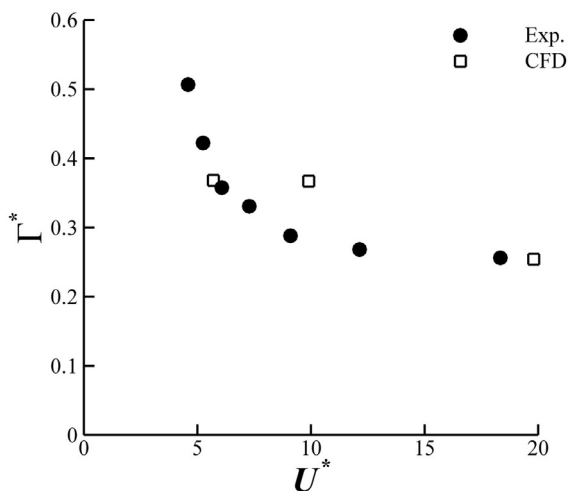(a) experiments and (b) prediction (h/D_i = 0·25, δ^*/D_i = 0·11).

Figure 8. Comparison of predicted and measured vortex circulation under crosswind conditions as a function of velocity ratio ($h/D_l = 0\cdot25$, $\delta^*/D_l = 0\cdot11$).

Figure 9. Comparison of predicted and measured DC60 under crosswind conditions as a function of velocity ratio ($h/D_l = 0\cdot25$, $\delta^*/D_l = 0\cdot11$).

The measured non-dimensional vortex circulation shows a monotonic rise in the vortex strength with decreasing velocity ratio i.e. increasing crosswind velocity for a fixed intake massflow (Fig. 8). When a critical velocity ratio is reached the ground vortex no longer forms as the sucked streamtube lifts off the ground. For the experiments the lowest velocity ratio at which a vortex is measured is $U^* = 4\cdot6$. The predicted vortex strength (Γ^*) shows reasonable agreement with the measurements with exceptional agreement at the low velocity ratio of approximately 5·7. The predicted circulation at the interim U^* of 9·9 is substantially over-predicted. There is no clear reason for this difference and is somewhat surprising as there is no fundamental change to the flow field in comparison to that at the lower velocity ratio of 5·7. Within previously published literature the effect of velocity ratio on the crosswind vortex strength has been the subject of conflicting reports. Some workers postulated that a higher velocity ratio would result in a stronger ground vortex[16]. However, Brix et al[17] reported quantitative results for crosswind configurations which showed that the vortex strength increased with reducing velocity ratio, within the intake duct. This is in agreement with the current experimental and computational results. Transient start-up studies of the formation mechanism in crosswind showed that the ground vortex forms in the near wake region of the intake and is associated with the vorticity of the separated shear layer on the outer surface of the intake. For a fixed intake Mach number, the velocity ratio is reduced by increasing the freestream velocity which consequently increases the intake near wake vorticity and subsequently leads to the formation of a stronger vortex. However, this is ultimately limited by the associated reduction in the sucked streamtube size which eventually results in the non-formation of the ground vortex.

Although there are appreciated limitations to the use of the distortion descriptor DC_{60} for such flows, there is no established alternative distortion parameter in widespread use. DC_{60} comparisons show reasonable agreement between the predictions and the experiments with the CFD typically underpredicting the DC_{60} in comparison with the measurements (Fig. 9). The intake distortion characteristic is similar to that of the vortex strength parameter with DC_{60} coefficient increasing as the velocity ratio reduces. This is not surprising as for most of the configurations the total pressure loss at the fan face is primarily driven by the vortex itself. However, there is a sharp rise in DC_{60} at a velocity ratio below about 5. This is primarily driven by the increasing size and depth of the windward lip
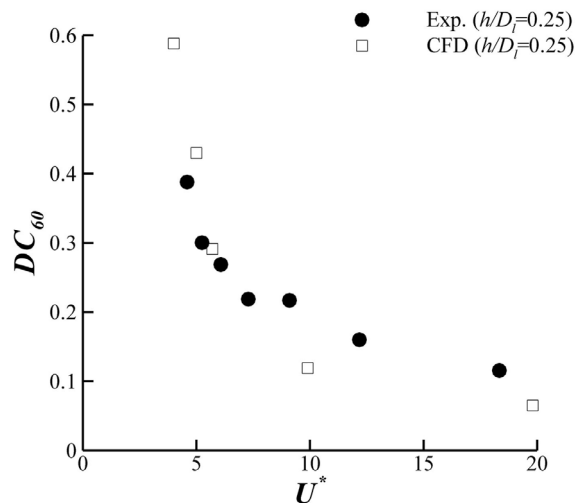
separation inside of the intake which indirectly affects the ground vortex as well as directly affecting the total pressure distribution itself. This lip separation occurs prematurely when in close proximity to the ground and subsequently also affects the characteristics of the ground vortex itself.

4.3 Effect of Reynolds number

Simulations were performed to investigate the pertinence of the experimental and computational results based on the scale-intake to a full-scale configuration. A set of predictions was realised for a full-scale model of the current geometry i.e. an inner intake diameter of 3·0m. The corresponding Reynolds number increased from $1\cdot26 \times 10^6$ to $3\cdot78 \times 10^7$ based on inner intake diameter and average intake velocity. Due to the changes in the Reynolds number, spatial discretisation in the near-wall region was modified to keep the y^+ wall distance in an acceptable range. The simulations show that non-dimensional vortex circulation changes by a maximum of about 5% and that the non-dimensional ground vortex characteristics under crosswind conditions are essentially independent of Reynolds number in the investigated range (Fig. 10).

The total pressure distortion coefficient DC_{60} is also unaffected in two of the three investigated configurations ($U^* = 9\cdot9$ and 19·8). At the lower velocity ratio of 5·7, the full-scale predictions show a reduction in total pressure distortion at the fan face by about 45%. In this configuration the DC_{60} is dominated by the effect of flow separation at the inlet lip of the scale intake and for the full-scale configuration this lip flow separation is delayed due to increased Reynolds number. Although DC_{60} is a conventional parameter for considering flow distortions it is limited with respect to vortical flows. Consequently, it is of interest to examine other distortion parameters and for this case the SC_{60} has also been calculated for both model-scale and full-scale predictions (Fig. 11). This highlights that there is very little difference between the model-scale and full-scale configurations which is as expected given that principal parameters of δ^*/D_l, h/D_l and U^* are conserved. Similar to the predicted and measured DC_{60} characteristics (Fig. 10(b)), as the velocity ratio reduces the SC_{60} increases. As U^* reduces, the critical point is eventually reached whereby the sucked streamtube lifts away from the surface and a clear ground vortex is not formed. However, although the ground vortex is removed there is a large separation on the windward intake lip which results in the monotonic
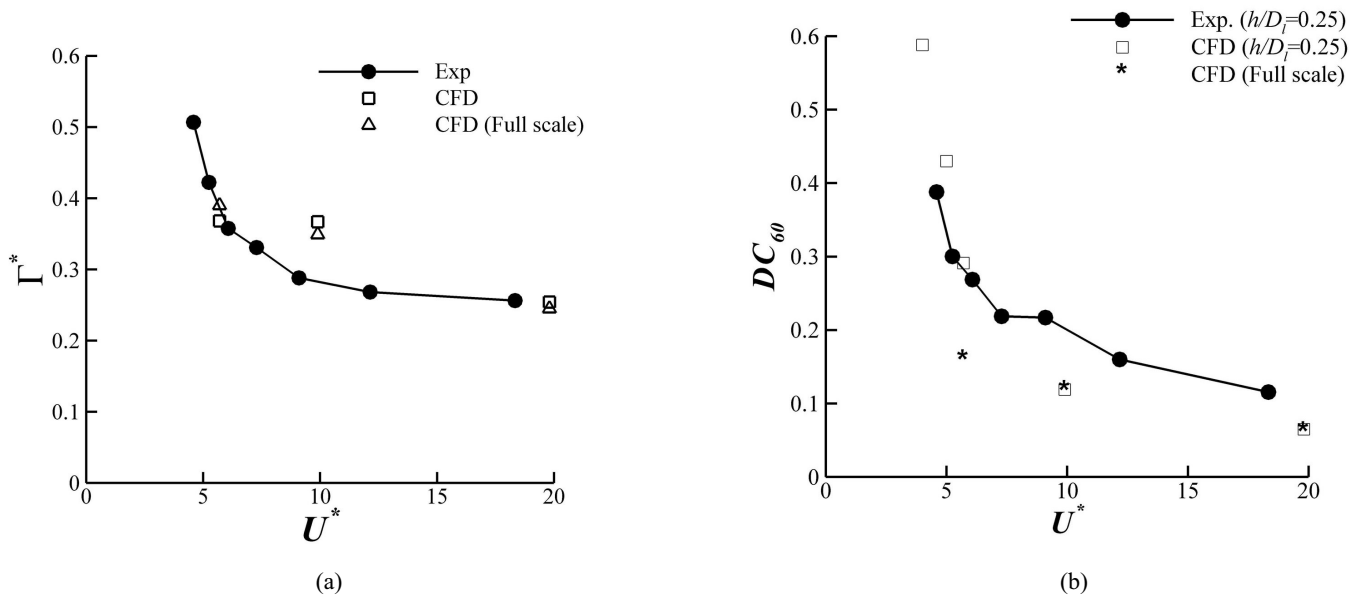
Figure 10. Comparison of predicted and measured vortex circulation (a) and DC_{60} (b) under crosswind conditions as a function of velocity ratio including full-scale predictions ($h/D_l = 0.25$, $\delta^*/D_l = 0.11$).

rise in DC_{60} as U^* reduces further. Figure 11 shows a sharp drop in SC_{60} when the critical velocity ratio is reached ($U^* \approx 5$). This is because a strong ground vortex no longer forms and highlights the difference between the DC_{60} and the SC_{60} parameters and how they can be used to reflect different distortion characteristics.

5.0 HEADWIND RESULTS AND DISCUSSION

5.1 Basic flow features and topology

Under headwind and quiescent conditions the ground vortex formation mechanism is known to be primarily dependent on the concentration and amplification of the ambient and suction induced ground based vorticity[4]. The vortex system generally consists of two counter-rotating ground vortices which are ingested into the intake. The sense of rotation of the vortices depends on the velocity ratio. At high velocity ratios or quiescent conditions the vortex formation is dominated by the suction induced boundary layer flow which convects from underneath the intake. This results in the formation and ingestion of a pair of contra-rotating vortices which are orientated as shown in Fig. 12(a)-(c). As the headwind speed increases and the velocity ratio reduces, the ingested vorticity is dominated by that bound in the approaching boundary layer. This results in a stronger contra-rotating vortex pair with an opposite sense of rotation (Fig. 12(d)-(f)). When the freestream velocity becomes sufficiently high and the velocity ratio reduces further, the sucked streamtube no longer interacts with the approaching boundary layer and the ground vortex system does not form.

A visualisation of the ground plane surface streaklines for a time averaged flow field shows a complex system of nodes, saddle points, separations and reattachments (Fig. 13). In this example for $U^* = 9.9$ and $h/D_l = 0.25$, the bounding edge of the sucked streamtube is clearly identifiable and the system comprises a balancing set of four saddle points and four nodes (Fig. 13(a)-(b)). The nodes are evenly divided between two stable foci (F1, F2) and two unstable isotropic source nodes (N1, N2). As expected, the saddle points (S1 and S2)
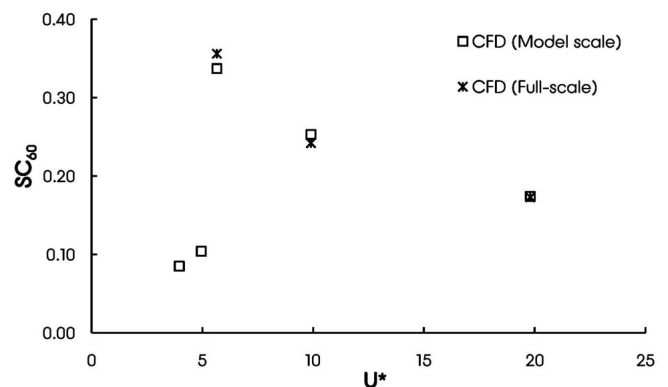

Figure 11. Predicted in-duct SC_{60} as a function of velocity ratio under crosswind conditions ($h/D_l = 0.25$, $\delta^*/D_l = 0.11$).

are associated with the edge of the ingestion domain and are directly connected along their attachment separators through the N1 source node. The N2 source node is also organised as part of a node-saddle-node arrangement along the attachment separators with S3 and S4. The footprints of the two symmetric ground vortices are associated with the foci points. While keeping the same velocity ratio ($U^* = 9.9$), as the ground clearance is increased there is a change to the surface flow streakline structure (Fig. 13(c)). Although the side saddle points (S1 and S2), primary node (N1) and the bounding streakline are similar the near-field region is different. The ground vortex foci (F1 and F2) are positioned further apart. The attachment node N2 and saddle point S4 do not occur and consequently the associated separation lines leading to F1 and F2 are also gone. The saddle point S3 is still evident.

The SPIV measurements were taken in a plane parallel to the ground and over an area of approximately 100mm wide and 85mm long which focused on obtaining measurements of the ground vortices. A comparison between the time-averaged CFD predictions
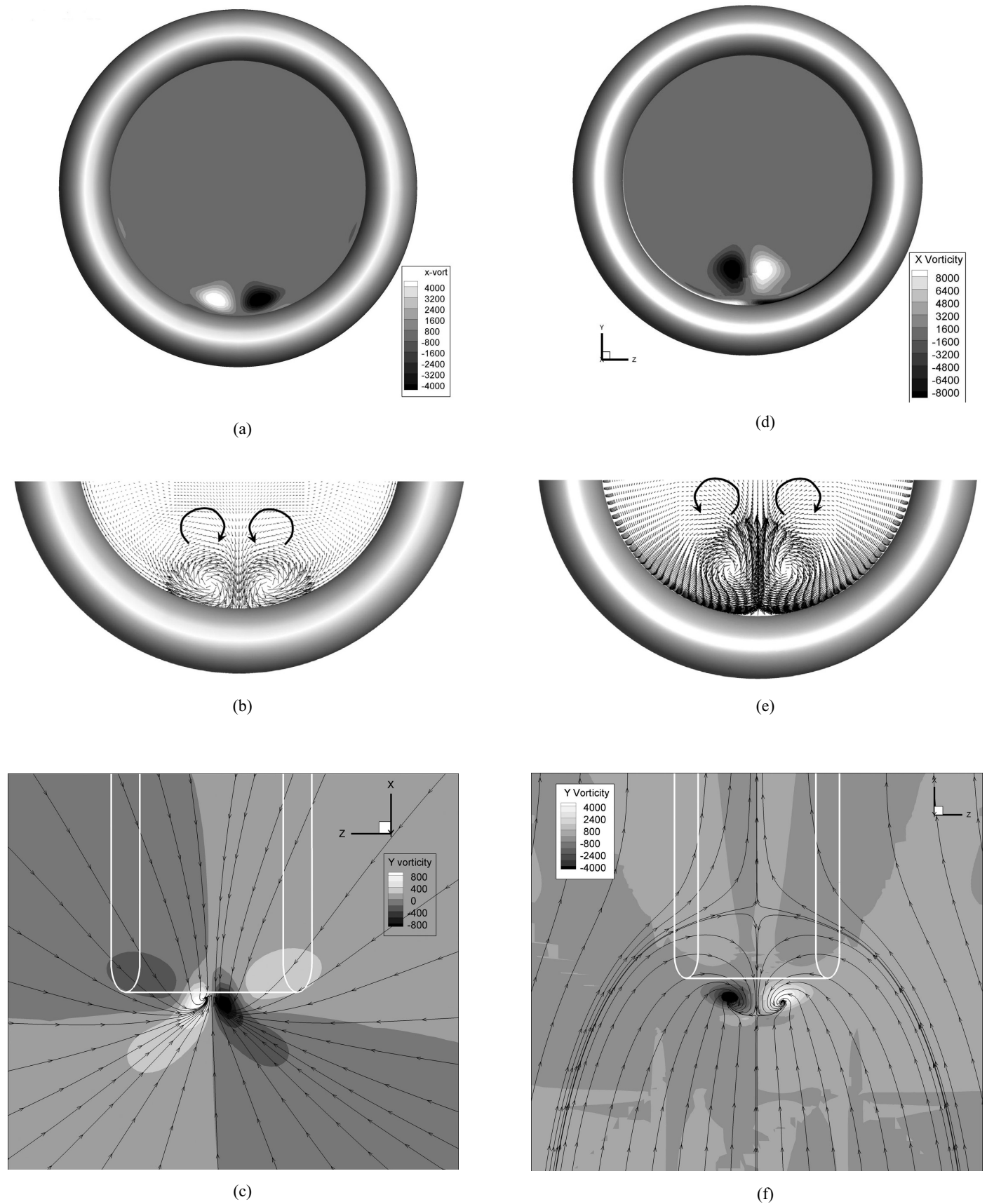
(a)

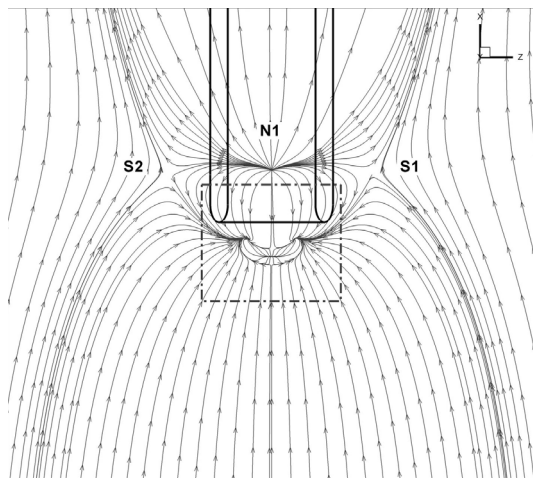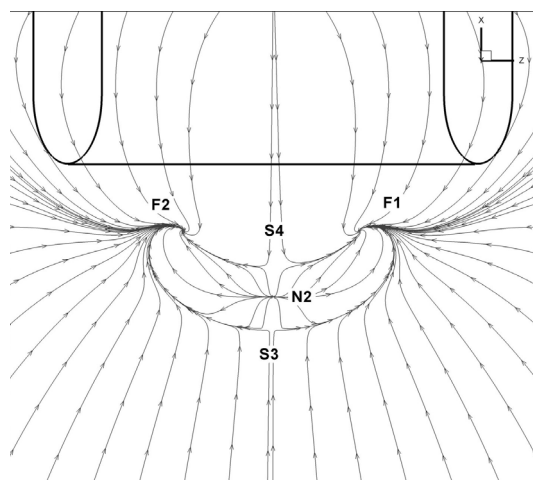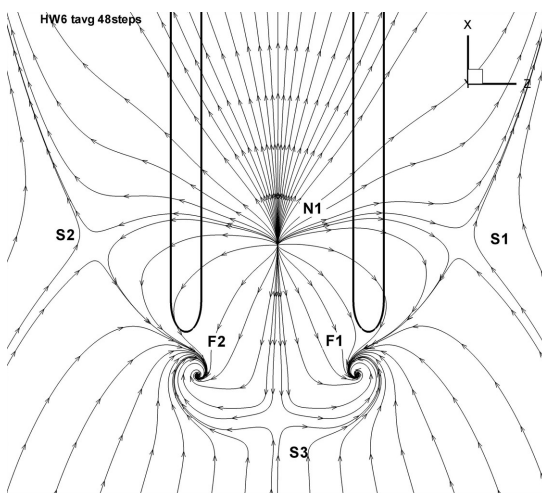(d)

(b)

(e)

(c)

(f)

Figure 12. Comparison between the time-averaged predicted ground vortex flow fields under (a)-(c) quiescent conditions ($U^* = \infty$, $h/D_l = 0.21$) and (d)-(e) headwind condition ($U^* = 9.9$, $h/D_l = 0.25$). (a) and (d) contours of ω_x, (b) and (e) velocity vectors, (c) and (f) contours of ω_y and bound streaklines in the PIV y-plane.
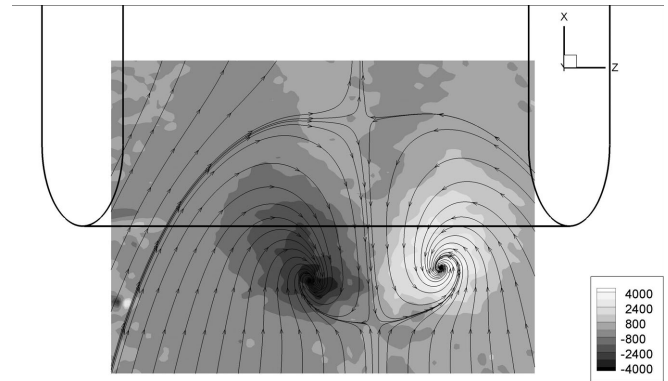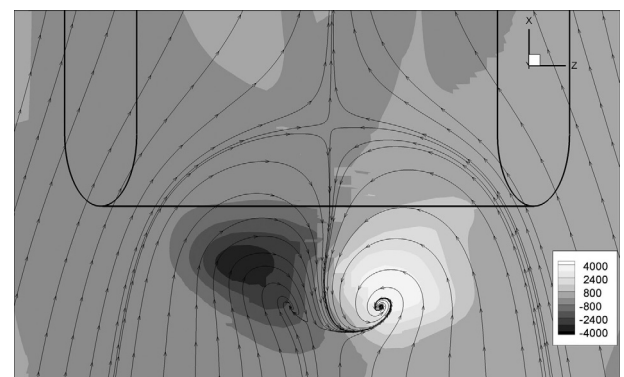
(a)

(b)

(c)

Figure 13. Predicted time-averaged ground plane surface streaklines for headwind conditions (a) overview (h/D_l = 0·25, U_l/U_∞ = 9·9) (b) near field region (h/D_l = 0·25, U_l/U_∞ = 9·9) (c) near field region (h/D_l = 0·40, U_l/U_∞ = 9·9).

(a)

(b)

Figure 14. Comparison of the time-averaged vorticity (ω_y) and two-dimensional streaklines in the PIV measurement plane (a) measurements and (b) CFD. Headwind configuration ($U_l/U_\infty \approx 5·0$, h/D_l = 0·25).

and the measurements for a headwind case ($U^* \approx 5·0$, h/D_l = 0·25) show similar flow structures with a pair of contra-rotating vortex foci and a saddle point positioned between the intake and the ground (Fig. 14). The strength of the vortices is at the same level although the predicted spacing is larger and the spatial locations are slightly different. The extent of the vortical regions is overpredicted in the CFD simulations, which was also observed under crosswind conditions. Grid convergence studies demonstrated that vortex core radii become smaller with increased grid resolution and therefore the effectively limited spatial discretisation of the grid appears to play a key role for this observation. Finally, the slight asymmetry in the predicted flow is due to the non-integral number of time-steps per flow period.

5.2 Unsteady aspects

Under most headwind conditions the flowfield was predicted to be unsteady. This is in agreement with the SPIV measurements which exhibited strong unsteadiness which was depended on the velocity ratio and ground clearance[2]. The experiments showed that for many headwind condition, the flow oscillates between a range of states of both vortex pairs as well as modulating single vortex modes[2]. The resulting movement in the vortex core location depends on the velocity ratio and as U^* decreases there is an increase in the vortex movement. Similarly as the ground clearance decreases the range of vortex movement was also found to increase[2]. Similar effects are observed in the CFD predictions where for some of the configurations the unsteadiness produces a
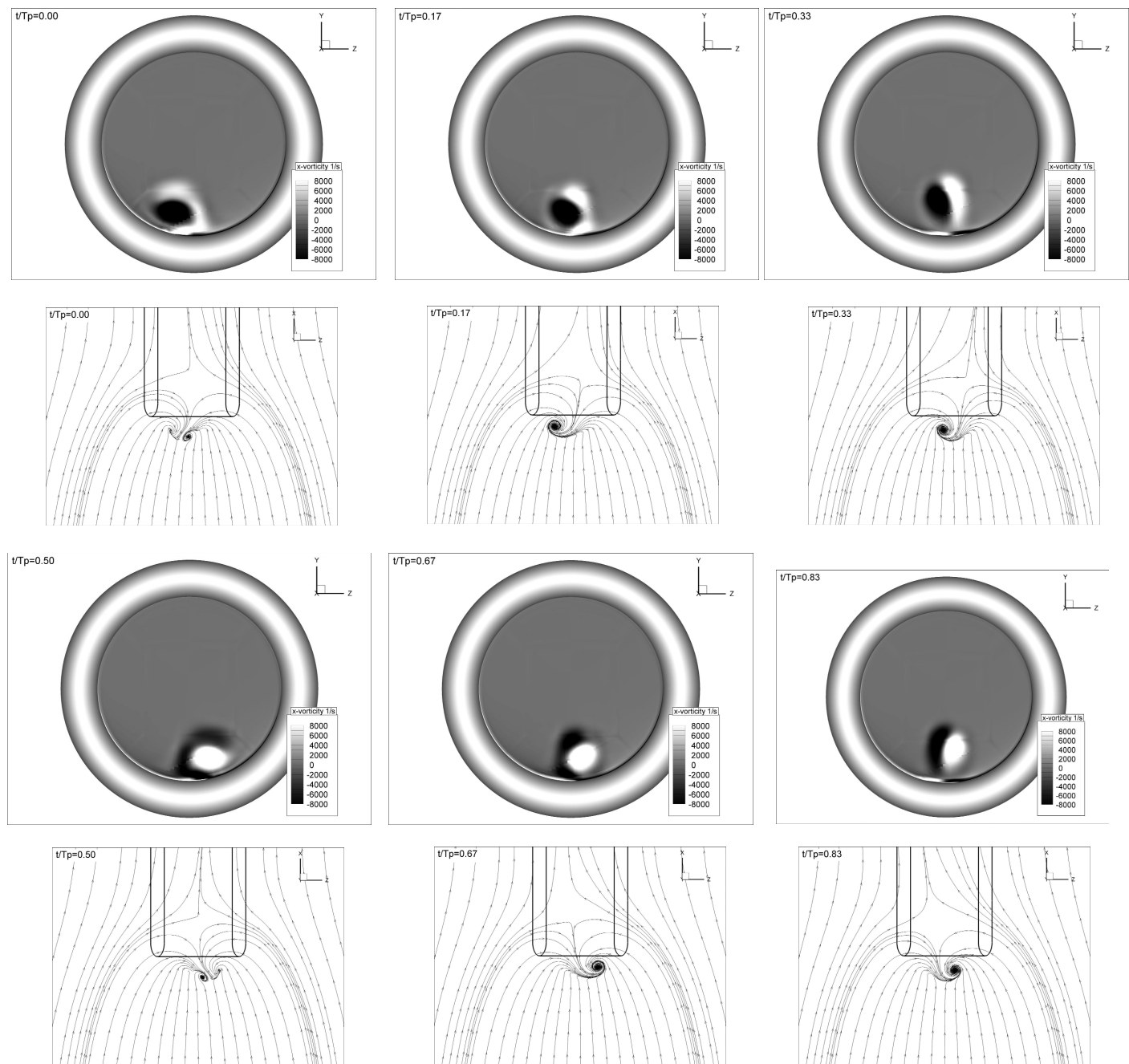
Figure 15. Unsteady flow modes in the PIV measurement plane and within the duct for a headwind configuration.
Contours of ω_x and velocity streaklines in the PIV plane ($U^* = 9\cdot9$, $h/D_l = 0\cdot25$).

periodic oscillation whereby the contra-rotating vortex pairs alternate in dominance and position. This occurs both within the intake as well as in the footprint of the vortices on the ground. This is highlighted in Fig. 15 which shows the streaklines in the PIV measurement plane as well as the in-duct ω_x contours for a sequence of snapshots through an oscillatory period. In this case, the flow dominant oscillations occur at about 14Hz (St = 0·007) and the sequence shows the development through one period. As well as illustrating the unsteadiness that occurs in the external flow, it highlights that these oscillations also occur for the ingested vortices within the duct. The flow development shows that the dominant vortex oscillates from one orientation to the other with a symmetric contra-rotating flow mode in between. This is mirrored within the duct where there is a small lag

between the in-duct flow and the features predicted in the plane external to the duct.

These unsteady characteristics are affected by both the ground clearance and the velocity ratio. For the same h/D_l of 0·25 but with a reduced velocity ratio of 5·0, the flow becomes more unsteady. In this case the flow is not a simple oscillation but is predicted to comprise two main frequency elements. Firstly, there is the familiar lateral oscillation of the flow as it switches from one side to the other – with a symmetric contra-rotating system in between. Secondly, at a much lower frequency, the flow changes to a different mode whereby a single vortex dominates for a period before ultimately switching back to the symmetric lateral oscillations. This is highlighted in Fig. 16, which shows a selection of snapshots of the predicted velocity streaklines in the horizontal plane.
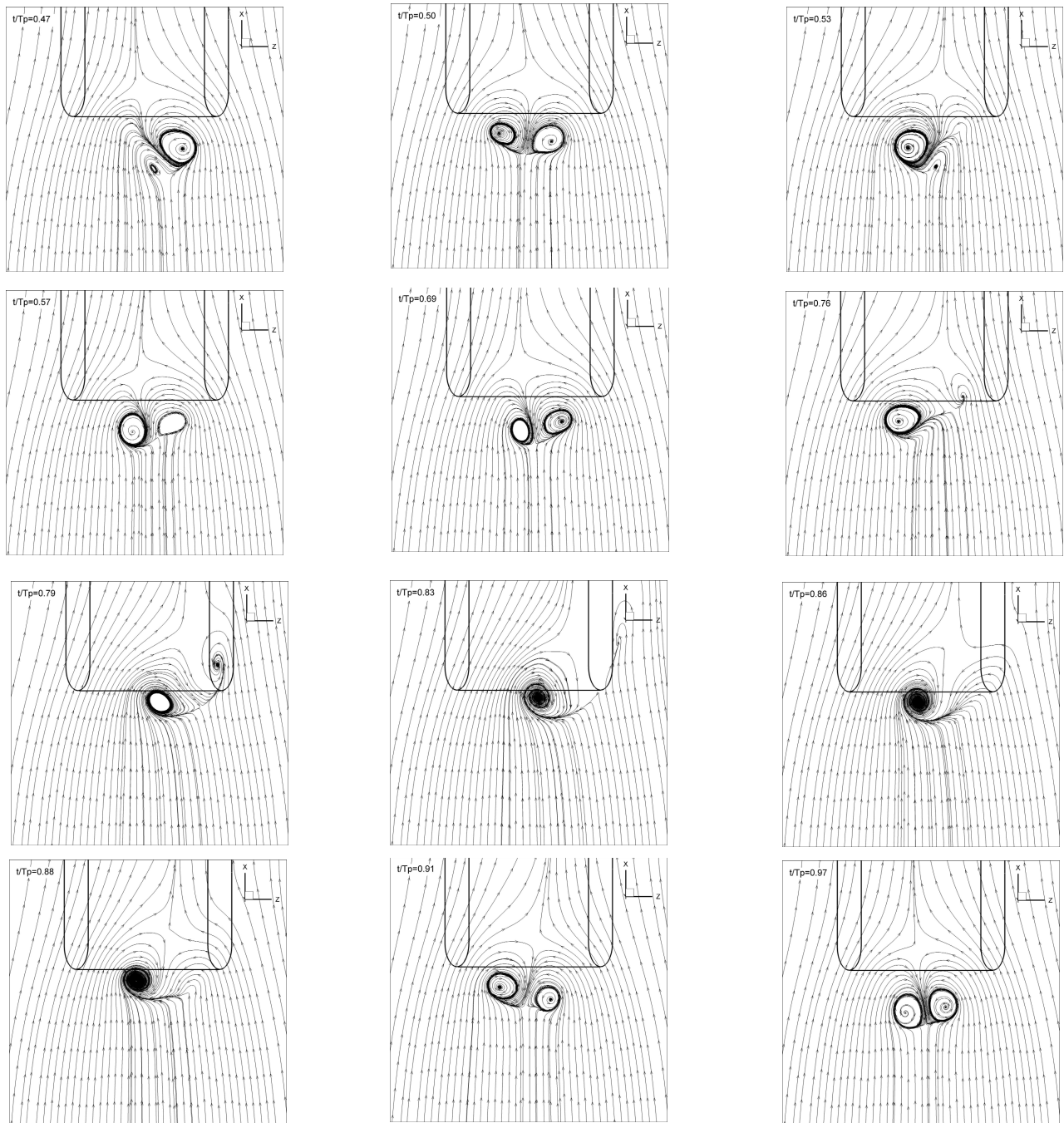
Figure 16. Unsteady flow modes in the PIV measurement plane for a headwind configuration ($U^* = 5\cdot0$, $h/D_l = 0\cdot25$).

This predicted unsteadiness is investigated by performing a spectral analysis of the flow variation at a specific location within the duct. For each configuration a point in the aerodynamic interface plane within the duct was chosen close to the centre of one of the ingested vortices. A Fourier transformation of the time-history shows the spectral content and the frequency is non-dimensionalised in terms of a Strouhal number. Due to the different power spectral density characteristics, the PSD amplitude is non-dimensionalised by the maximum value for each time series. For the ground clearance of $h/D_l = 0\cdot25$, the frequency peaks change with velocity ratio but are generally less than St = $0\cdot02$ (Fig. 17). For the U^* of $9\cdot9$ the simple peak is observed at St = $0\cdot007$. For the lower velocity ratio of $5\cdot0$, the flow is more complex as illustrated in Fig. 16. This is reflected in the PSD distribution which shows two distinct regions of spectral

peaks (Fig. 17(a)). The pair of peaks with Strouhal numbers between $0\cdot017$ and $0\cdot20$ is associated with the side-to-side oscillation of the primary vortex pair and the low frequency peaks with a Strouhal number of less than $0\cdot005$ is associated with the larger scale distortion which occurs when one of the vortices becomes temporarily dominant as seen in Fig. 16. Finally, for the lowest velocity ratio of $U^* = 4\cdot0$ the flow again becomes more simply periodic with a clearly dominant oscillation at St = $0\cdot007$ (Fig. 17(a)). The predicted unsteadiness frequency is only slightly affected by the change in ground clearance where the primary spectral peak increases from St = $0\cdot0074$ to $0\cdot0084$ when h/D_l increases from $0\cdot25$ to $0\cdot40$ (Fig. 17(b)). Furthermore, at this increased ground clearance the higher harmonics are also clearer at St $\approx 0\cdot016$ and $0\cdot024$. An extension of these results to a full scale configuration can be
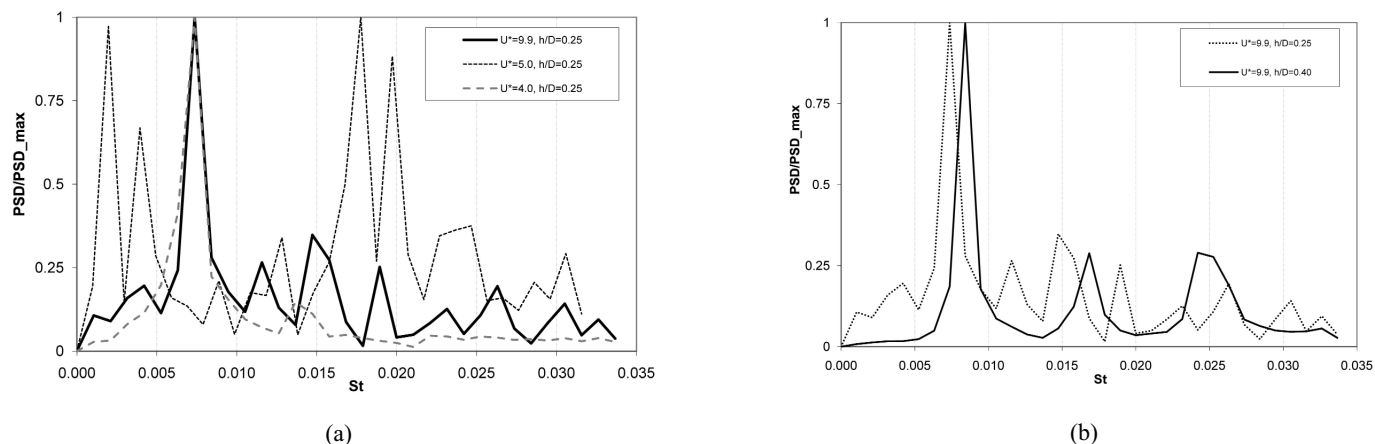
Figure 17. Spectral content of unsteady flow within the duct (a) effect of velocity ratio for $h/D_I = 0·25$ (b) effect of h/D_I for $U^* = 9·9$
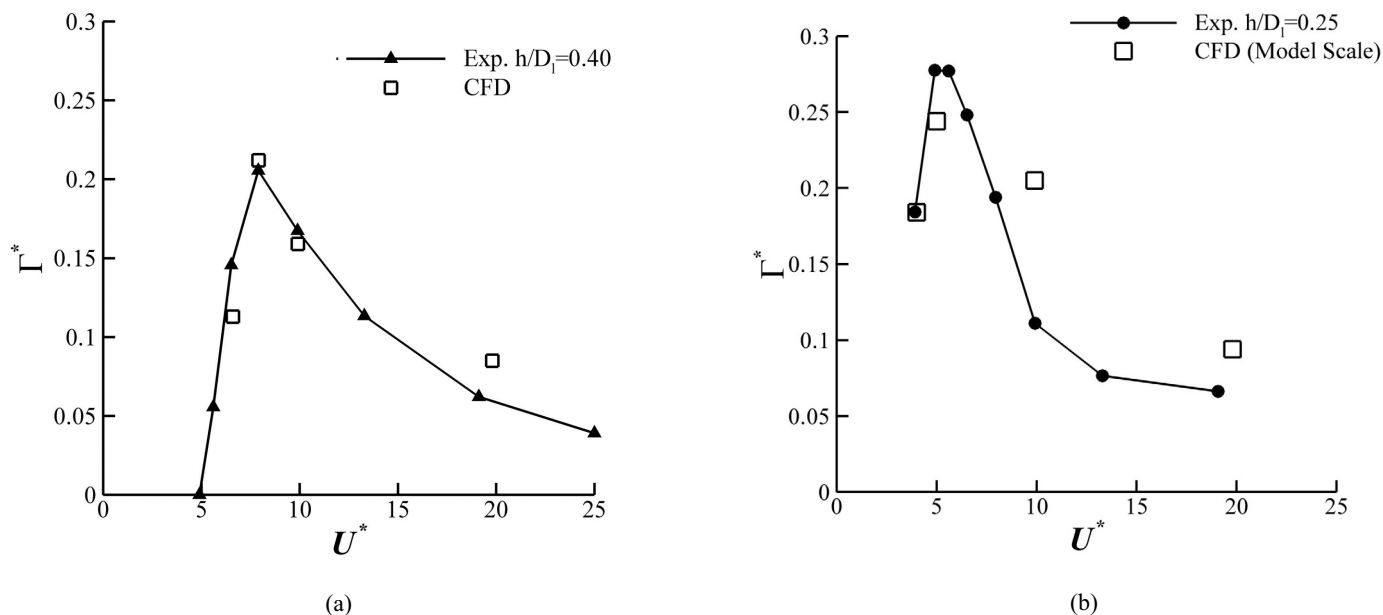

Figure 18. Comparison between experiments and predictions for the vortex circulation
as a function of velocity ratio under headwind conditions (a) $h/D_I = 0·40$ (b) $h/D_I = 0·25$.

considered simply based on the Strouhal number. This indicates that the vortex unsteadiness occurs at a very low frequency relative to the fan blade rotation. This is an important observation as one of the key aspects for this flow field is the possible detrimental effect on the fan vibration. Consequently, it is postulated that the effect of the ingested vortices on the fan aerodynamics could be analysed by using a 'frozen' prediction of the ground vortex.

These observations are in agreement with the ILES calculations of Karlsson & Fuchs[13] who showed similar frequency characteristics although with finer temporal resolution. The authors investigated a configuration which – according to the current definition – corresponds to $h/D_I \approx 0·6$ and $U^* = 10$. Four different modes of the vortex system connected by transition phases have been reported in this study. Some modes are dominated by relatively low frequencies, whilst other show relatively high frequency oscillations. The most intense of the low frequencies in the spectrum are in terms of Strouhal number in the range between approximately 0·006 and 0·045, which agrees well with the spectral content shown in Fig. 17.

5.3 Circulation and DC_{60} under headwind conditions

Quantitative comparison between the predictions and the experiments again focuses on the total ground vortex circulation and the total pressure distortion at the fan face in terms of DC_{60}. Under headwind conditions the circulation of the vortex system – the sum of the absolute circulation of both vortices – has been considered. The source of vorticity for ground vortex formation under headwind condition is dominated by the circulation in the approaching boundary layer of the ingested flow. For a fixed intake massflow (as in these studies), this approaching vorticity of the system increases as the headwind velocity increases with the concomitant reduction in velocity ratio and size of the sucked streamtube. As the velocity ratio reduces there is initially an increase in the vortex strength until a local maximum is reached beyond which Γ^* then reduces rapidly. This behaviour is caused by the competing effects of two different mechanisms. The vorticity within the boundary layer of the approaching flow increases as the velocity ratio reduces while at the same time the
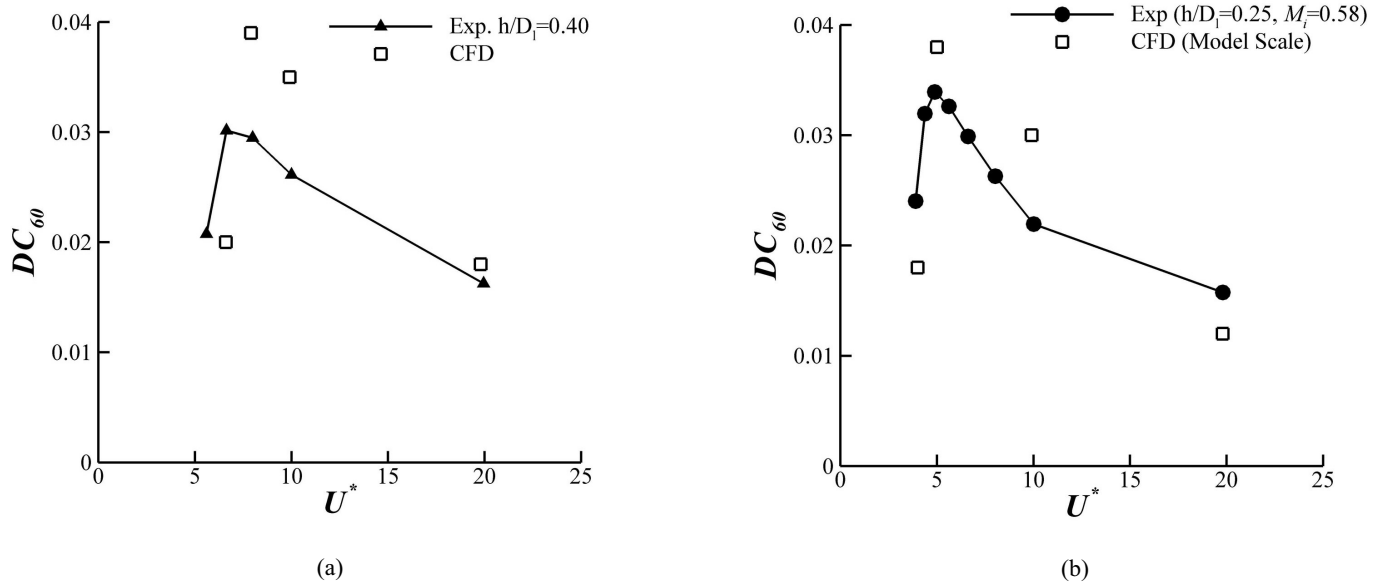
Figure 19. Comparison between experiments and predictions for the distortion parameter DC_{60} as a function of velocity ratio under headwind conditions (a) $h/D_i = 0.40$ (b) $h/D_i = 0.25$.

interaction with the ground is reduced as the streamtube contracts. Ultimately, the streamtube becomes small enough so that it lifts away from the surface and the ground vortices no longer form. At a ground clearance of $h/D_i = 0.40$ the CFD predictions capture these trends well with the peak circulation magnitude within 4% of the measurements (Fig. 18(a)). For the lower ground clearance ($h/D_i = 0.25$), the agreement is not as good although the trend of increasing vortex strength with reducing velocity ratio is observed (Fig. 18(b)). Furthermore, the predicted magnitude of the peak vortex strength is within 14% of the measured values.

The DC_{60} distributions show the same basic characteristics as the vortex strength with DC_{60} initially increasing as the velocity ratio is reduced which reaches a local maximum before subsequently decreasing again (Fig. 19). The agreement between the CFD and the measurements is mixed. The CFD again predicts the overall trends in agreement with the measurements and shows the local maximum DC_{60} followed by a rapid decrease as the velocity ratio reduces and the sucked streamtube gets smaller. However, the difference between the CFD and the measured DC_{60} is up to a 30% overprediction. There are also some cases where the CFD underpredicts the DC_{60}.

Both the vortex strength, Γ^*, and the distortion, DC_{60}, are slightly sensitive to the ground clearance h/D_i. As h/D_i is reduced from 0.40 to 0.25 the measured peak vortex strength increases from 0.21 to 0.28 and there is a decrease in the associated $(U^*)_{max}$ from 7.9 to 5.0 (Fig. 18). For intermediate values of U^* the vortex strength is greater when the intake is further from the ground. Finally, for large velocity ratios ($U^* = 20$) there is almost no effect of h/D_i on Γ^*. Similar trends are also observed for DC_{60} as a function of U^* and h/D_i. This observed increase in peak vortex strength and the reduction in the corresponding velocity ratio for the lower h/D_i are expected trends. Due to the lower ground clearance there will be a greater interaction of the sucked streamtube with the ground plane, enabling a vortex to form at lower velocity ratios (i.e. higher headwind velocities). With vortex formation being possible at higher headwind speeds, the greater levels of approaching boundary-layer vorticity inherent to these larger headwind speeds leads to a higher peak vortex strength as the velocity ratio further reduces. However, for intermediate velocity ratios the underlying mechanism for the observed sensitivity with ground clearance is unclear. The flowfield will be affected by a number of factors such as the ground induced intake flow, the primary sources of vorticity and the interaction between the ground plane and the sucked streamtube shape. Within this transitionary region, the topology changes from being dominated by flow from underneath and behind the intake to a flowfield principally controlled by the approaching upstream flow. The overall balance between these aspects results in a stronger vortex system for a larger ground clearance at these intermediate velocity ratios.

It is worth noting that the peak vortex strength under headwind conditions is about half of that experienced under crosswind conditions (Fig. 10(a)). Furthermore, DC_{60} is reduced by more than an order of magnitude from 0.4 in crosswind (Fig. 10(b)) to 0.035 under the most severe headwind conditions. This is driven by the twin effects of the crosswind vortex being larger in diameter but also the vortex total pressure loss in the duct is up to 20 times greater.

6.0 CONCLUSIONS

A combined computational and experimental study has been performed to improve the understanding of ground vortex formation and characteristics. The flow field has been investigated for both headwind and crosswind configurations and the effect of ground clearance has also been considered.

Under crosswind condition a single ground vortex is present, which is accompanied by a trailing vortex system which consists of two vortices – one inside and one outside of the sucked streamtube. The near field trailing vortex (inside of the capture streamtube) is also ingested in the intake. The crosswind ground vortex strength monotonically increases as the velocity ratio decreases. When a critical velocity ratio is reached the ground vortex no longer forms as the sucked streamtube lifts off the ground. Under most headwind conditions the flowfield is unsteady and the unsteady characteristics are affected by both the ground clearance and the velocity ratio. For many headwind conditions, the flow oscillates between a range of states of both vortex pairs as well as modulating single vortex modes. Under these headwind conditions, the circulation of the vortex system increases as the velocity ratio reduces until a local maximum is reached beyond which circulation then reduces rapidly.

This behaviour is caused by the competing effects of the increasing amount of vorticity in the ground boundary layer and the reducing cross section of the capture streamtube.

The unsteady RANS predictions have been compared with non-intrusive flow velocity measurements as well as with in-duct total pressure surveys and the associated distortion descriptors. The CFD captures the basic trends of the ground vortex flow fields for both headwind and crosswind conditions. Good quantitative agreement is found for many configurations although there are some headwind arrangements where there are notable discrepancies between the predictions and the measurements. Relative to the previous understanding, this has enabled a revised flow model for the crosswind configurations to be proposed and described.

ACKNOWLEDGEMENTS

REFERENCES

1. JOHNS, C. The aircraft engine inlet vortex problem, 2002, AIAA Paper 2002-5894.
2. MURPHY, J. Intake Ground Vortex Aerodynamics, 2008, PhD thesis, Cranfield University.
3. NAKAYAMA, A. and JONES, J. Correlation for formation of inlet vortex, *AIAA J*, 1998, **37**, (4), pp 508-510.
4. DE SIERVI, F., VIGUIER, H., GREITZER, E. and TAN, C. Mechanisms of inlet vortex formation, *J Fluid Mechanics*, 1982, **124**, pp 173-207.
5. BURLEY, C.L., BROOKS, T.F., VAN DER WALL, B., RICHARD, H., RAFFEL, M. and BEAUMIER, P., ET AL. Rotor wake vortex definition – initial evaluation of 3-C PIV results of the Hart-II Study, 2002, 28th European Rotorcraft Forum.
6. VATISTAS, G., KOZEL, V. and MIH, W.C. A simpler model for concentrated vortices, *Experiments in Fluids*, 1991, **11**, pp 73-76.
7. VAN DER WALL, B. and RICHARD, H. Analysis methodology for 3-C PIV data of rotary wing vortices, *Experiments in Fluids*, 2006, **40**, pp 798-812.
8. TAYLOR, J. *An Introduction to Error Analysis: The Study of Uncertainties in Physical Measurements*, University Science Books, 1982, California.
9. RAFFEL, M., WILLERT, C. and KOMPENHANS, J. *Particle Image Velocimetry: A Practical Guide*, 1998, Springer, Berlin.
10. PETRACCI, A., VAN DOORNE, C.W.H., WESTERWEEL, J. and LECORDIER, B. Analysis of stereoscopic PIV measurements using synthetic images, in: *Particle Image Velocimetry: Recent Improvements*, STANISLAS, M., WESTERWEEL, J. and KOMPENHANS, J. (EDS), 2003, Springer, Berlin.
11. PRASAD, A. Stereoscopic particle image velocimetry, *Experiments in Fluids*, 2000, **29**, pp 103-116.
12. ROACHE, P. Verification and validation, in *Computational Science and Engineering*, 1998, Hermosa, Albuquerque.
13. KARLSSON, A. and FUCHS, L. Time evolution of the vortex between an air inlet and the ground, 2000, AIAA Paper 2000-0990.
14. GREEN, J. Forced response of a large civil fan assembly, 2008, ASME Paper GT2008-50319.
15. GREEN, S. *Fluid Vortices*, 1995, Kluwer Academic Publishers, Dordrecht.
16. SHIN, H., GREITZER, E., CHENG, W., TAN, C. and SHIPPEE, C. Circulations measurements and vortical structure in an inlet-vortex flow-field, *J Fluid Mechanics*, 1986, **162**, pp 463-487.
17. BRIX, S., NEUWERTH, G. and JACOB, D. The inlet-vortex system of jet engines operating near the ground, 2000, AIAA Paper 2000-3998.